

Tropical Pacific intensifies June extreme rainfall over Southwestern United States/Northwestern Mexico

Honghai Zhang^{1,2,3}

Received: 15 November 2019 / Accepted: 8 May 2020 © Springer-Verlag GmbH Germany, part of Springer Nature 2020

Abstract

Extreme rainfall over Southwestern United States/Northwestern Mexico (SWUNWM) has been mostly investigated during wet seasons, while no or little attention has been paid to extreme rainfall during dry seasons despite its vital importance for sustaining vegetation and ecosystems. Here we examine the top 1% rainfall over SWUNWM in June, the driest month on average, and assess how it is affected by the ocean with a 50 km-resolution global climate model. Comparing millennia-long simulations with and without the ocean, we find that the ocean does not change the pattern and magnitude of atmospheric circulation associated with June extreme rainfall, but significantly enhances rainfall intensity. This intensification is attributed to a larger variability of atmospheric moisture content enhanced mainly by the sea surface temperature (SST) in the tropical Pacific. The similarities in the atmospheric circulation associated with, and the temporal characteristics of, June extreme rainfall between the two simulations point to a dominant control of extreme rainfall dynamics by atmospheric intrinsic processes and atmosphere-land coupling. These modeling results imply that the predictability of occurrence of June extreme rainfall over SWUNWM is limited by atmospheric intrinsic dynamics and atmosphere-land coupling, while reliable predictions of its intensity likely require a faithful simulation of SST variability, especially in the tropical Pacific.

Keywords Extreme rainfall · Rainfall intensity · Sea surface temperature variability · Atmospheric circulation · Atmospheric moisture content · Southwestern North America

1 Introduction

Extreme rainfall not only can cause severe floods (e.g., Neiman et al. 2011; Moore et al. 2011; Ralph et al. 2012), but also can terminate multiyear persistent droughts (Dettinger 2013, 2016) and provide vital water for vegetation and ecosystems during dry seasons (e.g., Notaro et al. 2010; Pascolini-Campbell et al. 2019). This dual role is especially evident over Southwestern North America (SWNA), where extreme rainfall dictates total annual precipitation and exhibits strong year-to-year variability (e.g., Dettinger et al. 2011; Cannon et al. 2018).

- Program in Atmospheric and Oceanic Sciences, Princeton University, Princeton, NJ, USA
- Geophysical Fluid Dynamical Laboratory/NOAA, Princeton, NJ, USA
- ³ Present Address: Lamont-Doherty Earth Observatory, Columbia University, Palisades, NY, USA

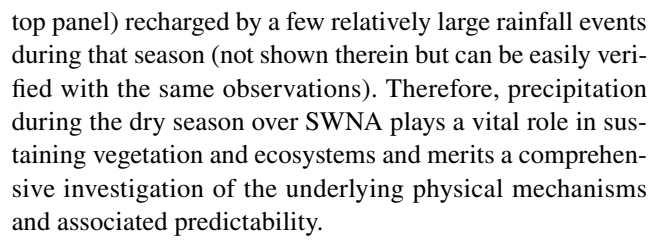
Published online: 19 May 2020

Past studies on extreme rainfall over SWNA have focused mostly on floods in wet seasons, either the North American Monsoon (NAM) season (July to Mid-September) over southwestern U.S. and northwestern Mexico (Adams and Comrie 1997; and references in Sect. 6) or the Mediterranean-type winter over the southern U.S. West Coast. In the monsoon season, extreme rainfall over SWNA is mostly related to easterly upper-level disturbances such as inverted troughs (e.g., Lahmers et al. 2016; and references therein), while anticyclonic Rossby wave breaking in the mid-latitude westerlies can also lead to heavy rainfall over the northern part of the monsoon region (Sierks et al. 2020). In winter, extreme precipitation along the U.S. West Coast is caused mainly by landfalling atmospheric rivers (AR) interacting with coastal orography (e.g., Ralph et al. 2004, 2006; Neiman et al. 2011); non-orographic secondary contributions include dynamic forcing and convective instability associated with changes in synoptic scale atmospheric circulation (Cannon et al. 2018). These studies highlight the role of atmospheric intrinsic processes in extreme precipitation over SWNA.



Ocean–atmosphere coupled variability in the tropics has also been shown to modulate extreme precipitation over SWNA via large-scale atmospheric Rossby waves (Hoskins and Karoly 1981). On seasonal to interannual timescales, many studies have presented observational and numerical evidence that El Niño-Southern Oscillation (ENSO) can impact the frequency, intensity, location and moisture source of extreme precipitation over SWNA (e.g., Higgins et al. 2000; Andrews et al. 2004; Bao et al. 2006; Schubert et al. 2008; Corringham and Cayan 2019), but debate still exists especially in terms of ENSO's quantitative impacts and associated predictability on local scales (e.g., Bracken et al. 2015; Cannon, 2015). On decadal and longer time scales, the tropical Pacific SST low-frequency variability has been linked to the observed delay in the monsoonal rainfall and associated extremes in recent decades (e.g., Grantz et al. 2007). Atlantic multidecadal variability has also been shown to affect weather extremes over North America (e.g., Curtis 2008; Ruprich-Robert et al. 2018). On intraseasonal and shorter timescales (<90 days), tropical intraseasonal variability such as the Madden-Julian Oscillation has been shown to play a significant role in the SWNA extreme precipitation (e.g., Higgins et al. 2000 and references therein; Jones and Carvalho 2012, 2014; Stan et al. 2017; Zheng et al. 2018) and impact its prediction skills (Jones et al. 2010, 2011). Most of these studies, if not all, focused on the SWNA extreme precipitation during the wet seasons.

In contrast, extreme precipitation during dry seasons over SWNA—the top few percentiles of dry-season only precipitation—has received little or no attention. This is presumably because extreme events during dry seasons nearly always have a weaker amount of rainfall than those during wet seasons and do not qualify when all-season precipitation is used to identify extremes. In fact, precipitation during the dry season over SWNA has overall received very little attention in the literature (Pascolini-Campbell et al. 2019). However, dry season precipitation over SWNA, including extremes, is vital for sustaining vegetation and ecosystems (e.g., Notaro et al. 2010; Pascolini-Campbell et al. 2019). Vegetation growth and ecosystem productivity over SWNA are largely water-limited and depend mainly on soil moisture supplied by precipitation (Notaro et al. 2010). During the dry season (i.e., spring to early summer), lack of precipitation causes soil moisture to persistently decrease by transpiration leading to a seasonal decline in vegetation greening and ecosystem productivity (Pascolini-Campbell et al. 2019, Fig. A1). This dry-season climate pattern can change, however, with a few relatively large rainfall events. For example, Pascolini-Campbell et al. using ecosystemlevel site observations in southwestern U.S., show that the ecosystem productivity during the dry season (May-June) of 2009 is conspicuously higher than other dry seasons and is associated with anomalously high soil moisture (their Fig. 5,



In this work, we focus on the dry-season extreme precipitation over SWNA, and in particular, we use a high-resolution global climate model to investigate how the ocean, specifically SST variability, affects the dry-season extreme precipitation. We find that the largest impacts of SST variability on the dry-season extreme precipitation are simulated in June over a SWNA region around 32°N–34°N and 113°W–116°W, encompassing southern California and Arizona of the U.S. and northern Baja California and Sonora of Mexico (hereafter SWUNWM). Next, we focus on this SWUNWM region and illustrate how SST variability affects June extreme precipitation in the model.

2 Model and experiments

The global climate model used here is the Forecast-oriented Low Ocean Resolution (FLOR) flux-adjusted model (Vecchi et al. 2014) developed at the Geophysical Fluid Dynamics Laboratory (GFDL). FLOR has a high horizontal resolution of approximately 50 km for the atmosphere (AM2.5) and land (LM3) components and a horizontal resolution of 1° (telescoping to 0.333° near the equator) for the ocean (MOM4) and sea ice (Sea Ice Simulator) components. The flux-adjustment in FLOR imposes fixed anomalous enthalpy, momentum and fresh water fluxes (varying seasonally but not interannually) to the ocean to bring its long-term climatology of SST and wind stress closer towards observational estimates over 1979–2012. This bias correction in global SST and wind stress mean state also leads to improvements in the simulations of global precipitation and atmospheric teleconnections (Jia et al. 2014; Pascale et al. 2016; Zhang and Delworth 2018a) and many regional climate features such as tropical cyclones (TCs) up to category 3 hurricanes (Vecchi et al. 2014), the NAM (Pascale et al. 2016, 2017) and South/North American hydroclimate (Zhang et al. 2016; Zhang and Delworth 2018b).

Over the SWNA region, FLOR simulates a realistic spatial distribution of precipitation climatology in June, especially the minimum around the SWUNWM region and the maximum associated with the incipient NAM to the southeast (Fig. 1a, b). Over the SWUNWM region (Fig. 1c), the observed precipitation climatology (Schneider et al. 2011; Harris et al. 2014) features a bimodal annual cycle with two maxima in February (~15.0 to 16.4 mm, winter-storm precipitation) and August (~14.8 to 16.9 mm, monsoonal



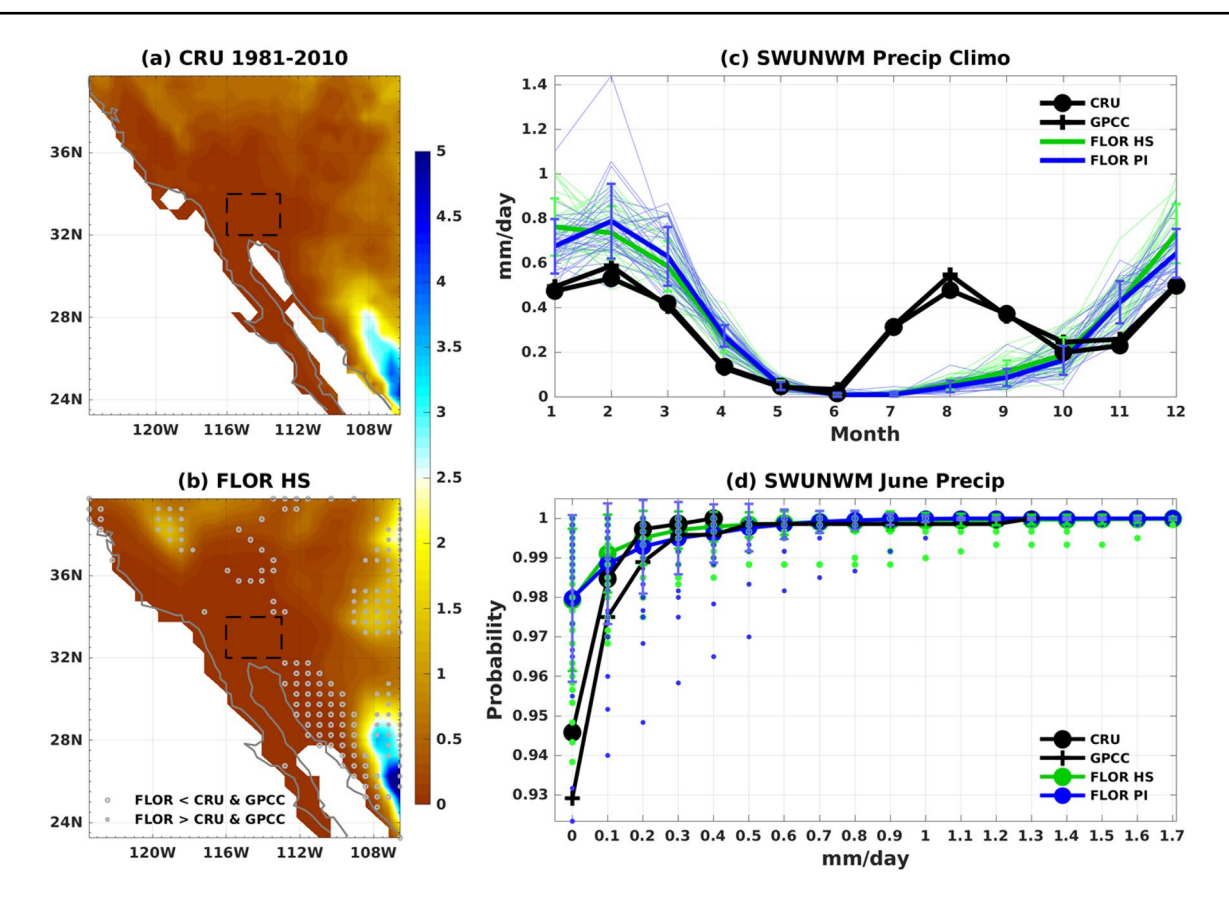


Fig. 1 Model evaluation. **a** Observed June precipitation climatology for 1981–2010 from Climatic Research Unit Timeseries (CRU TS) 0.5° precipitation datasets version 3.24.01. Dashed black box indicates the SWUNWM area, 32°N–34°N and 113°W–116°W. **b** FLOR simulated June precipitation climatology in the 35-member historical simulations (FLOR HS) used in Zhang and Delworth (2018a, b). Gray stippling indicates that FLOR either overestimates (filled dots) or underestimates (open circles) the observed climatology, based on comparing the CRU and GPCC climatology with the 35-member ensemble FLOR HS; overestimation is defined when all 35 members are larger than both CRU and GPCC, and vice versa. **c** Climatological annual cycle of precipitation averaged over SWUNWM in observa-

tions, CRU (black with dots) and Global Precipitation Climatology Centre version 2018 (GPCC, at 0.5° resolution, black with crosses), and in FLOR HS (green) and preindustrial simulation (FLOR PI) used here (blue). For FLOR, thin and heavy curves are the individual members and the ensemble mean, respectively. The FLOR PI ensemble has 33 members of non-overlapping 30 years constructed from the 1000-year FLOR simulation. **d** Cumulative probability distribution of June precipitation over SWUNWM based on grid-point data (i.e., not area-averaged) in CRU, GPCC, FLOR HS and PI (small dots are the individual ensemble members). Vertical bars in **c**, **d** denote the 1 standard deviation of the FLOR HS and PI ensembles. Precipitation in all panels has the unit of mm/day

precipitation) and two minima in June (~0.4 to 1.0 mm) and October (~6.1 to 7.6 mm), respectively, and June is the driest month for the area. This annual cycle over SWUNWM is fairly well simulated in FLOR from October to June (observations inside the model spread), but from July to September the enhanced monsoonal rainfall is not captured in FLOR. This bias is presumably due to the fact that the NAM in FLOR, despite its realistic simulation over the monsoon core region (see Fig. 1 of Pascale et al. 2017), does not penetrate as far north as in observations during the monsoon season. However, this bias from July to September does not degrade the performance of FLOR in simulating June rainfall over SWUNWM, because even

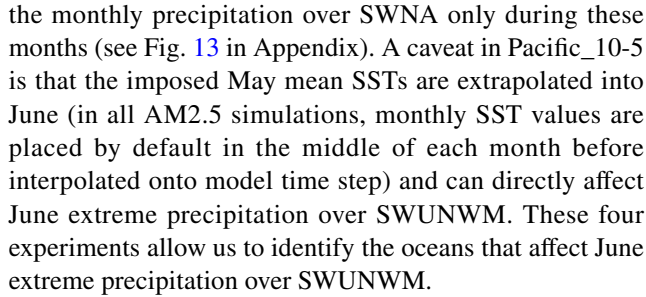
in observations the monsoon has not reached this region in June (Fig. 1a). Further justifications for use of the model are that FLOR realistically simulates the statistical distribution of June mean precipitation across the SWUNWM area (Fig. 1d, observations inside the 1 standard deviation range of the model spread, except at 0 mm/day) as well as the daily characteristics and physical processes associated with the strongest June rainfall events in reanalysis products (see Sect. 3 below).

To investigate the role of SST variability in June extreme rainfall over SWUNWM, we first compare two long simulations, one conducted with the fully coupled



FLOR for 3500 years and the other with the uncoupled AM2.5 for 1000 years (note in AM2.5, atmosphere is still coupled with land). Both simulations are driven by preindustrial level atmospheric composition and radiative forcing. In the AM2.5 simulation (hereafter AM2.5), the boundary forcing is prescribed as the climatological annual cycle of monthly mean SST and sea ice (concentration and thickness) derived from the last 1000 years of the FLOR simulation. This 1000-year FLOR simulation (hereafter FLOR) is used in the comparison with AM2.5 while the remaining years are only used for cross-validation. FLOR and AM2.5 share the same radiative forcing and the same climatology at the surface, but differ in that the ocean (including sea ice) is fully active in FLOR but does not exist in AM2.5. Comparing these two millennium-long simulations allows a clean and robust assessment of how the ocean affects extreme precipitation.

To provide further insights on which parts of the ocean affect extreme precipitation, we analyze four additional 600-year AM2.5 simulations. These simulations are conducted for a companion study focusing on the large-scale interannual variability of North American precipitation, but are found to shed light on the local extreme rainfall investigated here. They are similar to the above AM2.5 simulation except that time-varying monthly mean SSTs from FLOR are imposed in different regions and times. The first one has monthly SSTs prescribed over the entire globe (for all months, hereafter, Globe_1-12) to test whether this technique (AM2.5 imposed with monthly SSTs) can reproduce the FLOR precipitation variability over land [over the ocean, interactive ocean-atmosphere coupling matters (e.g., He et al. 2017, 2018)]. The other three have monthly SSTs prescribed between 35°N and 35°S in the entire tropics for all months (Tropic_1-12), the tropical Pacific for October to May (Pacific 10-5) and the tropical Atlantic for May to October (Atlantic_5-10), respectively. Tropic_1-12 can test the role of SSTs in the tropics versus extratropics, while Pacific_10-5 and Atlantic_5-10 can test the role of SSTs in the tropical Pacific from October to May and in the tropical Atlantic from May to October, respectively. The reason for prescribing SSTs only during the selected months in Pacific_10-5 and Atlantic_5-10 is that the Pacific and Atlantic SSTs in FLOR are found to correlate significantly with



In this work, extreme precipitation is defined as the Junes when June mean precipitation amount over SWUNWM is above its 99th percentile and thus 10 Junes are selected from each 1000-year simulation. Although choosing a lower threshold (such as the 90th percentile commonly used in studies with limited data) allows more samples, it does not affect the mechanisms presented here.

3 Results

We start by examining the timeseries of simulated June mean precipitation averaged over SWUNWM in FLOR (last 1000 years) and AM2.5 (Fig. 2). In June, precipitation in FLOR (blue curve) is very weak in most years; but occasionally in some years (e.g., Year 0184 and 0195) the SWUNWM area can receive a relatively large amount of rainfall, even comparable to the wet season (Feb) average (Fig. 1c). This feature in FLOR—most years extremely dry and occasionally relatively wet—is also simulated in AM2.5 without SST variability (red curve in Fig. 2); however, the intensity of June rainfall during the wet years is conspicuously weaker in AM2.5 than in FLOR. For example, the largest June rainfall in AM2.5 (Year 0230) among the 1000year simulation is still below the 99th percentile of June rainfall in FLOR. Next, we focus on the extreme years in which June rainfall amount is above the 99th percentile in each simulation, examine the physical processes underlying these extreme rainfall events and explain how SST variability intensifies June rainfall over SWUNWM.

Figure 3 shows the daily timeseries of precipitation in June over SWUNWM for the 10 extreme years in FLOR and AM2.5. Consistent with the June mean timeseries (Fig. 2), the amplitude of daily rainfall is overall larger in FLOR than in AM2.5. We note that, in both simulations, June precipitation comes mostly from one dominant rainfall event that appears to persist one to a few days. This temporal characteristic is consistent with that in the strongest June rainfall events in reanalysis products (Kanamitsu et al. 2002) (see Fig. 14 in Appendix). In addition, the two strongest events in reanalysis (1988 and 1999) exhibit daily rainfall of intensity comparable to that in FLOR. These similarities with reanalysis products on daily time scales provide validation



¹ Although the flux adjustment in FLOR is derived under present-day conditions, preindustrial radiative forcing is nearly in balance at top of the atmosphere and thus more suitable for millennium-long steady state simulations as done here. In addition, the difference in SST climatology between preindustrial and present-day levels is much weaker compared to the SST biases in the standard FLOR without flux adjustment. Therefore, the flux adjustment derived under present-day conditions still reduces the climatology biases in FLOR under preindustrial forcing.

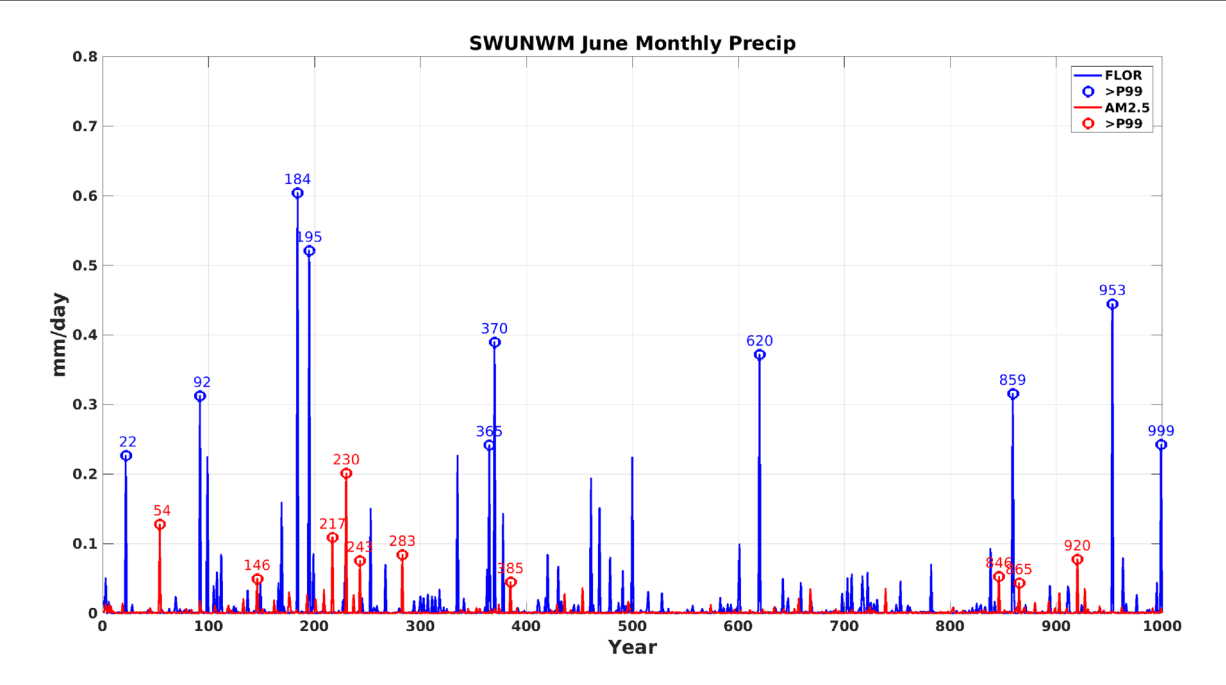


Fig. 2 Time series of June mean precipitation averaged over SWUNWM in FLOR (blue) and AM2.5 (red). Circles indicate the years in which June precipitation is above the 99th percentile in the FLOR (last 1000 years) and AM2.5 simulations, respectively

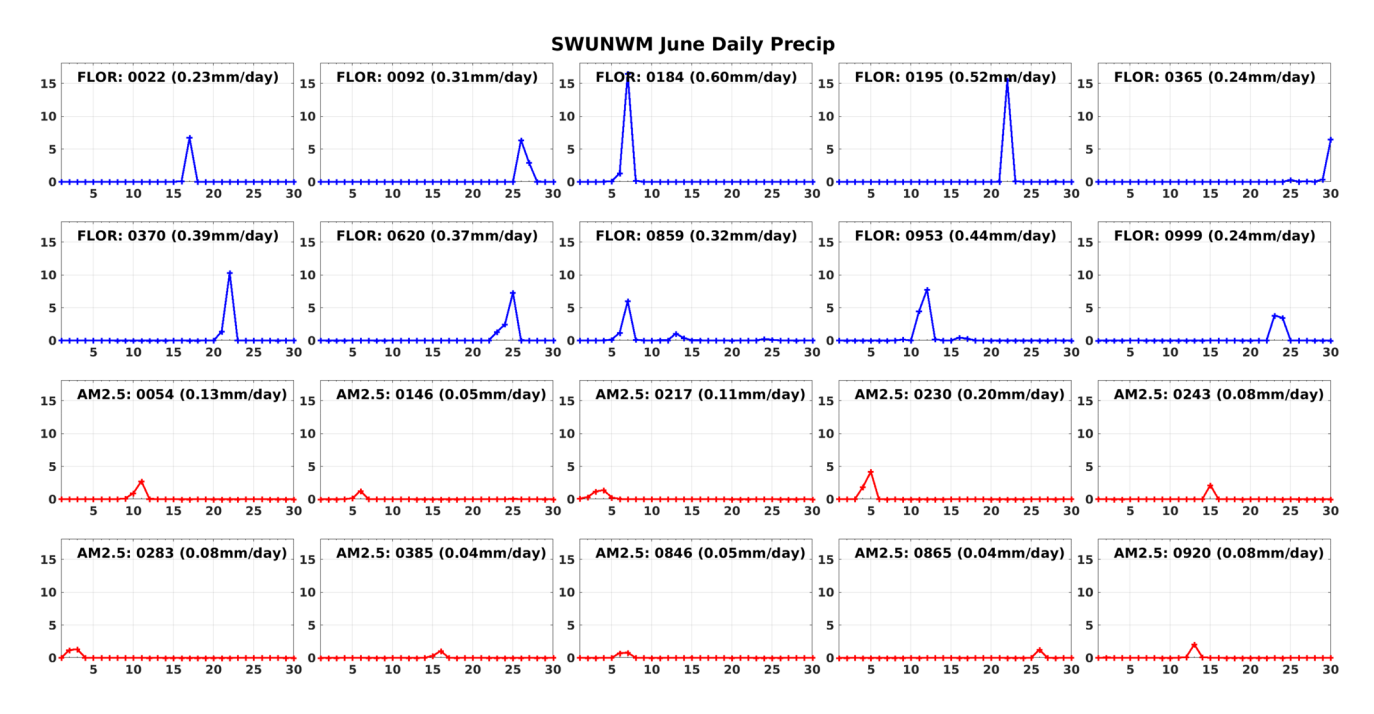


Fig. 3 Daily time series of June extreme rainfall events over SWUNWM defined in Fig. 2 for FLOR (top two rows, blue curves) and AM2.5 (bottom two rows, red curves). Labeled in each panel is

the model, year and June mean rainfall in mm/day (inside parentheses). The unit for y axis is mm and for x axis is day (of June). The range of y axis is the same for all panels

for the model's ability to simulate June precipitation over SWUNWM.

To show the average differences between FLOR and AM2.5 and also shed light on the atmospheric processes underlying the extreme June rainfall events, we first perform

a composite analysis of the 10 extreme events using daily mean outputs. Daily climatology is removed prior to the composite and events are aligned according to their rainfall peak. For years with more than one rainfall event in June (mostly in FLOR, such as Year 0859), the strongest event is



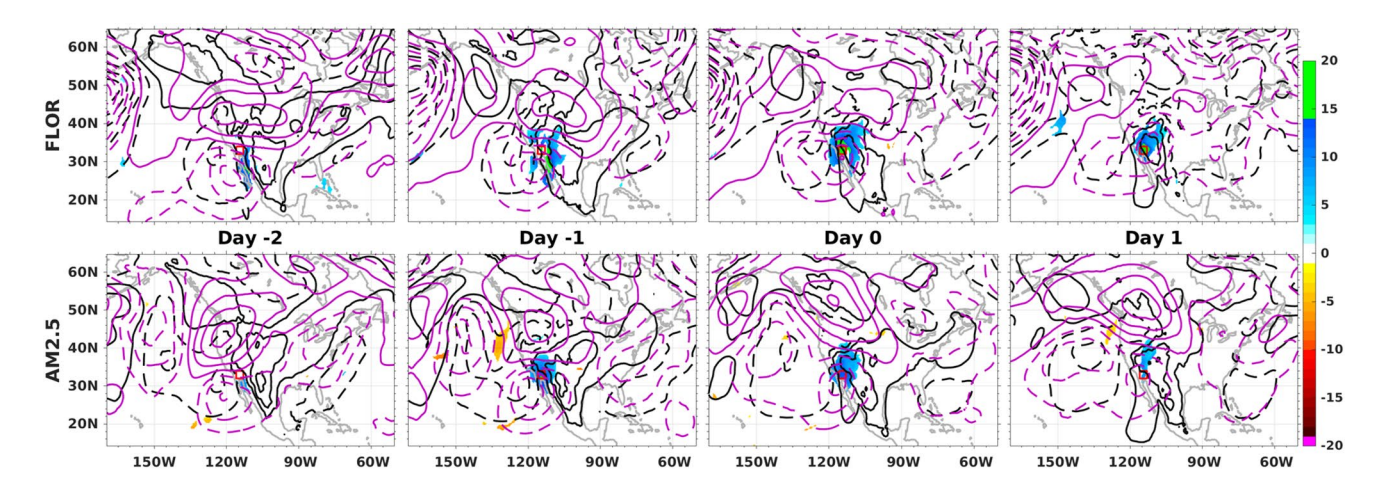


Fig. 4 Composite daily evolution of June extreme rainfall events over SWUNWM (defined in Fig. 2) from 2 days before the rainfall peak to 1 day after for FLOR (top row) and AM2.5 (bottom row). Shading denotes CWV anomalies (kg/m²) and only shows regions where the 10 extreme events have the same sign in their CWV anomalies, in which case the composite is defined robust. The compos-

ite CWV anomalies averaged over SWUNWM at Day 0 are about 20 kg/m² in FLOR and 12.6 kg/m² in AM2.5. SLP anomalies are in black contours (± 1 hPa, ± 3 hPa, ± 5 hPa, ...) and 500GH anomalies are in magenta contours (± 10 m, ± 30 m, ± 50 m, ...). For both, positive anomalies are solid and negative anomalies are dashed. The SWUNWM area is indicated in each panel by a red box

used in the composite. Figure 4 shows the composite evolution of extreme rainfall events in terms of column-integrated water vapor (CWV, shading), sea level pressure (SLP, black contours) and 500mb geopotential height (500GH, purple contours) from 2 days before the rainfall peak to 1 day after. During the evolution leading to the peak, the composite atmospheric circulation near SWUNWM exhibits very similar patterns and magnitudes between the fully coupled FLOR and the uncoupled AM2.5 without SST variability. Two days before the peak rainfall, the Gulf of California is sandwiched between positive SLP anomalies to the east over land and negative SLP anomalies to the west over the ocean. This composite SLP pattern drives strong anomalous southerly flow over the Gulf transporting moisture northward into the SWUNWM area, which is consistent with previous studies demonstrating the important contribution of moisture surges from Gulf of California to the precipitation over southwestern U.S. (Pascale et al. 2016; and references therein). Accompanying at 500mb are an anomalous cyclone to the south of SWUNWM and an anomalous anticyclone to the north. This composite pattern of atmosphere circulation persists until the peak of the extreme rainfall events, with the surface anomalous anticyclone moving slightly westward and the 500mb anomalous cyclone moving northward. At the peak of the events over SWUNWM, there are positive SLP anomalies but negative 500GH anomalies. The composites of SLP and 500GH in FLOR are very similar to those in reanalysis products (see Fig. 15 in Appendix), which provides process-level validation for FLOR's ability to simulate June precipitation events over SWUNWM. Note that the evolution of atmosphere circulation in the composite does not necessarily appear in all individual events (not shown).

Despite the differences among individual events, the similar pattern and magnitude of the composite atmosphere circulation between FLOR and AM2.5 suggests that SST variability does not significantly change the atmosphere dynamic processes associated with the extreme rainfall events in June over SWUNWM.

In contrast to the atmosphere circulation, the composite CWV is noticeably different between FLOR and AM2.5 (Fig. 4). Specifically, the robust (all 10 events have the same sign) positive CWV anomalies near SWUNWM in FLOR are significantly (at 5% level based on the one-sided t-test) larger than those in AM2.5 throughout the development of extreme rainfall events. For instance, the CWV anomalies averaged over SWUNWM at Day 0 are about 20.0 kg/m² in FLOR versus 12.6 kg/m² in AM2.5. These differences in CWV are consistent with the stronger intensity of extreme rainfall events in FLOR than in AM2.5. Considering the similarities in atmosphere circulation associated with extreme rainfall events and the similar CWV climatology (see Fig. 17 in Appendix) between FLOR and AM2.5, we infer that positive atmospheric moisture content anomalies are enhanced by SST variability and are responsible for larger atmospheric moisture convergence and thus the stronger intensity of June extreme precipitation over SWUNWM in FLOR than in AM2.5.

To support this inference, we compare between FLOR and AM2.5 the variability of June mean CWV, vertically integrated divergence of June mean atmospheric winds in the troposphere below 500mb (a measure of the convergent circulation typically related to ascent and rainfall) and June mean precipitation minus evaporation (P-E) which is balanced by atmospheric moisture tendency and moisture flux



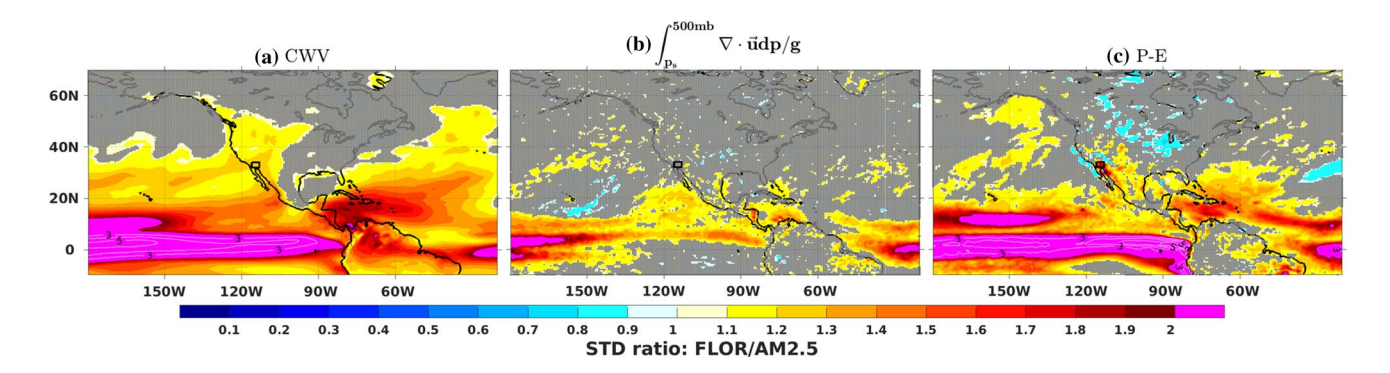


Fig. 5 FLOR to AM2.5 ratio of standard deviation in June mean **a** CWV, **b** vertically integrated (surface to 500 mb) divergence of atmospheric winds as a proxy for atmospheric circulation (divergent component) and **c** precipitation minus evaporation as a collective proxy for atmospheric moisture and circulation. Ratios larger than

2 are contoured in white. Gray stippling indicates that the standard deviation is not significantly different between AM2.5 and target simulations at the 1% significance level based on the F test. The SWUNWM area is indicated in each panel by a black box

convergence. Note that the contribution of submonthly transient eddies (important for the daily extremes considered here) is included in June mean P-E, but not directly in CWV and the lower tropospheric divergent circulation (e.g., Seager and Henderson 2013); hence these results using June mean fields should be interpreted carefully along with the above composite analysis using daily fields. Over the ocean, compared to AM2.5, SST variability in FLOR significantly (at 1% level based on the F-test) enhances the standard deviation (STD) of June mean CWV (Fig. 5a) in latitudes up to about 40°N/S (southern hemisphere not shown), but only enhances the STD of the lower tropospheric divergent circulation (Fig. 5b) in the tropics (mainly over warm waters). These differences both contribute to the STD differences in P-E over the ocean (Fig. 5c). Over the land near SWUNWM, the STD is significantly larger in FLOR than in AM2.5 for the atmospheric moisture content and P-E (Fig. 5a, c), but not for the atmospheric divergent circulation (Fig. 5b). These results, along with the composite analysis above, suggest that the stronger intensity of June extreme rainfall events over SWUNWM in FLOR is primarily due to the larger variability of atmospheric moisture content that is enhanced by SST variability, and that in this model the atmospheric circulation associated with extreme rainfall in June over SWUNWM is insensitive to SST variability.

In addition to the composite analysis, we also examine the evolution of each individual event in both FLOR and AM2.5 and focus on their sources of moisture. We aim to investigate whether SST variability, in addition to intensifying the variability of atmospheric moisture content, can change the moisture sources of June extreme rainfall events over SWUNWM. This question could be answered by a backward trajectory analysis tracking the water vapor sources of extreme rainfall events (e.g., Eckhardt et al. 2004; Bao et al. 2006). However, such an analysis would require high spatiotemporal resolution (on the order of hourly and several

tens of vertical levels) that is not available in our long simulations. Nonetheless, in order to gain some insights on this question, we assess the daily evolution of CWV anomalies for each individual event and the associated moisture contribution on the three levels that are available in both FLOR and AM2.5 (reference height of 10 m for winds and 2 m for specific humidity, 850mb and 500mb). For most of the events, we find that the propagation of CWV anomalies is not clear too far ahead of the rainfall peak; hence we limit the analysis to within a few days before the rainfall peak.

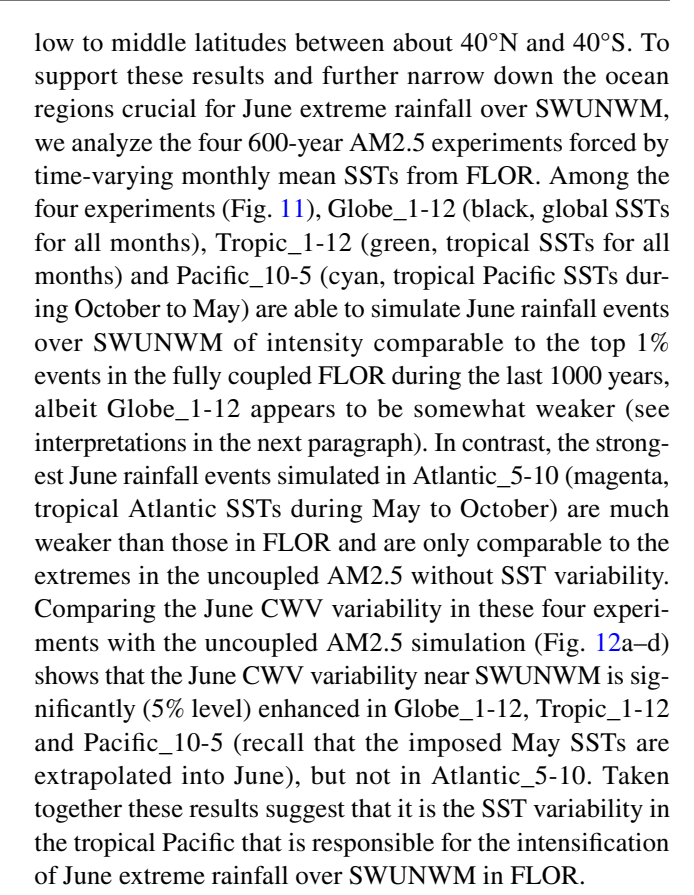
For 9 of the 10 extreme rainfall events in FLOR and all 10 events in AM2.5, the associated CWV anomalies appear to come from south of the SWUNWM area—either the northeastern tropical Pacific or the northwestern Mexico-around 3 or 4 days prior to the rainfall peak (see Table 1 in Appendix). For one event in FLOR (0999, Fig. 6 third row and Fig. 7), the CWV anomalies appear to be from northwest of the SWUNWM area about 2–3 days before the event peak. Note that a northwestern source of CWV over SWUNWM is also simulated in AM2.5 (not shown) but does not appear to contribute directly to the 10 extreme rainfall events examined here. For both FLOR and AM2.5, the CWV anomalies associated with extreme rainfall events over SWUNWM have moisture contributions from all three levels examined (Table 1 in Appendix). For example, in FLOR for Year 0022 the largest moisture contribution among the three levels is the moisture flux convergence at 500 mb (Fig. 8), while for Year 0620 the moisture contribution at 500 mb is weaker than those at reference height and 850 mb (Fig. 9). Overall, this analysis shows that the moisture sources of June extreme rainfall over SWUNWM appear to be similar between the fully coupled FLOR and the uncoupled AM2.5 and insensitive to SST variability.



ARs (atmospheric rivers) and TCs (tropical cyclones) are common causes of extreme rainfall over SWNA during wet seasons (e.g., Ralph et al. 2006). Here we find that ARs² and TCs likely also contribute to the extreme rainfall over SWUNWM during dry seasons. Among the extreme rainfall events examined here, one event (0999) in FLOR and two (0230, 0283) in AM2.5 appear to be associated with an AR (Table 1 in Appendix). For FLOR 0999 (Fig. 6 third row and Fig. 7) the AR propagates from northwest of the SWUNWM area, while for AM2.5 0230 (Fig. 6 fourth row and Fig. 10) the AR propagates from southwest of the SWUNWM area. In FLOR, three events (0195, 0370, 0620) appear to be associated with a TC formed over the eastern tropical Pacific (Table 1 in Appendix). For example, the TC associated with the event 0620 is indicated by a block of strong positive CWV anomalies (Fig. 6 second row) and cyclonic winds (Fig. 9) south of the Baja California (in its decaying phase) 4 days before the rainfall peak; after that (Day -3 to 0) its remnants enter the Gulf of California and propagate northward onto the SWUNWM area. In AM2.5, although none of the 10 events examined here is associated with a TC, AM2.5 still simulates TCs over the eastern tropical Pacific (not shown). In the reanalysis product (Fig. 14 in Appendix), one rainfall event (June 2, 1999) appears to be associated with an AR coming from southwest of the SWUNWM area (Fig. 16 in Appendix), while TCs are not found to contribute to the 5 strongest events during 1979–2020.

Two further questions arise concerning the role of SST variability in the intensification of June extreme rainfall over SWUNWM. First, are there patterns of SST variability in FLOR that are responsible for the intensification? A composite of monthly mean SST anomalies for the extreme events examined in FLOR does not reveal any robust (all 10 events have the same sign) SST anomalies several months leading to the events (not shown), which suggests that the intensification of June extreme rainfall over SWUNWM cannot be attributed to any specific SST variability.

Second, which parts of the ocean are crucial for the intensification of June extreme rainfall over SWUNWM? The results above (Fig. 5a) indicate that the variability of atmospheric moisture content is enhanced by SST variability in



June extreme rainfall over SWUNWM in Globe_1-12 appears overall weaker than that in the fully coupled FLOR during the same period (years 2601–3200, Fig. 11), although its June mean CWV variability over the ocean and the broad SWNA region has a magnitude most comparable to FLOR (relative to Tropic 1-12 and Pacific 10-5, Fig. 12a-c vs Fig. 5a). This paradox is likely due to the fact that rainfall depends both thermodynamically on atmospheric moisture and dynamically on atmospheric circulation. As shown above, while CWV variability is enhanced by SST variability, the atmospheric circulation associated with June extreme rainfall events over SWUNWM arises mainly from atmospheric intrinsic dynamics that are largely white noise (e.g., Shepherd 2014). The random nature of white noise dynamics implies that it is possible for SWUNWM to have an extended period of dry spell even with the presence of enhanced CWV variability. This interpretation has support from the 3500-year FLOR simulation. As shown in Fig. 11, FLOR simulates extended relatively dry (e.g., years 0330–1300, note the similarity with Globe_1-12) and relatively wet (e.g., 2500-3500) periods over SWUNWM, but has similar magnitudes of CWV variability between these periods (Fig. 12e). This feature in FLOR is also seen in the 1000-year uncoupled AM2.5 without SST variability: the top 1% June rainfall events over SWUNWM are clustered during the first 400 and last 200 years with a much drier period in between (see also Fig. 2) although the CWV



² ARs here refer to the atmospheric processes that resemble the typical wintertime ARs, which are characterized by an elongated narrow band of enhanced CWV and the associated low-level moisture transport along and within the band. The quantitative thresholds used in literature to identify wintertime ARs (e.g., 2 cm CWV in Ralph et al. 2004, 2006) are not used here because (1) they are based on total (climatology+anomaly) fields while here anomalous fields are used (2) climatologies are quite different between summer and winter, especially for CWV. Nonetheless, the characteristics of wintertime ARs are clear in the anomalous CWV and low-level (10 m, 850 mb, and 500 mb) moisture transport for FLOR 0999 and AM2.5 0230 and 0283.

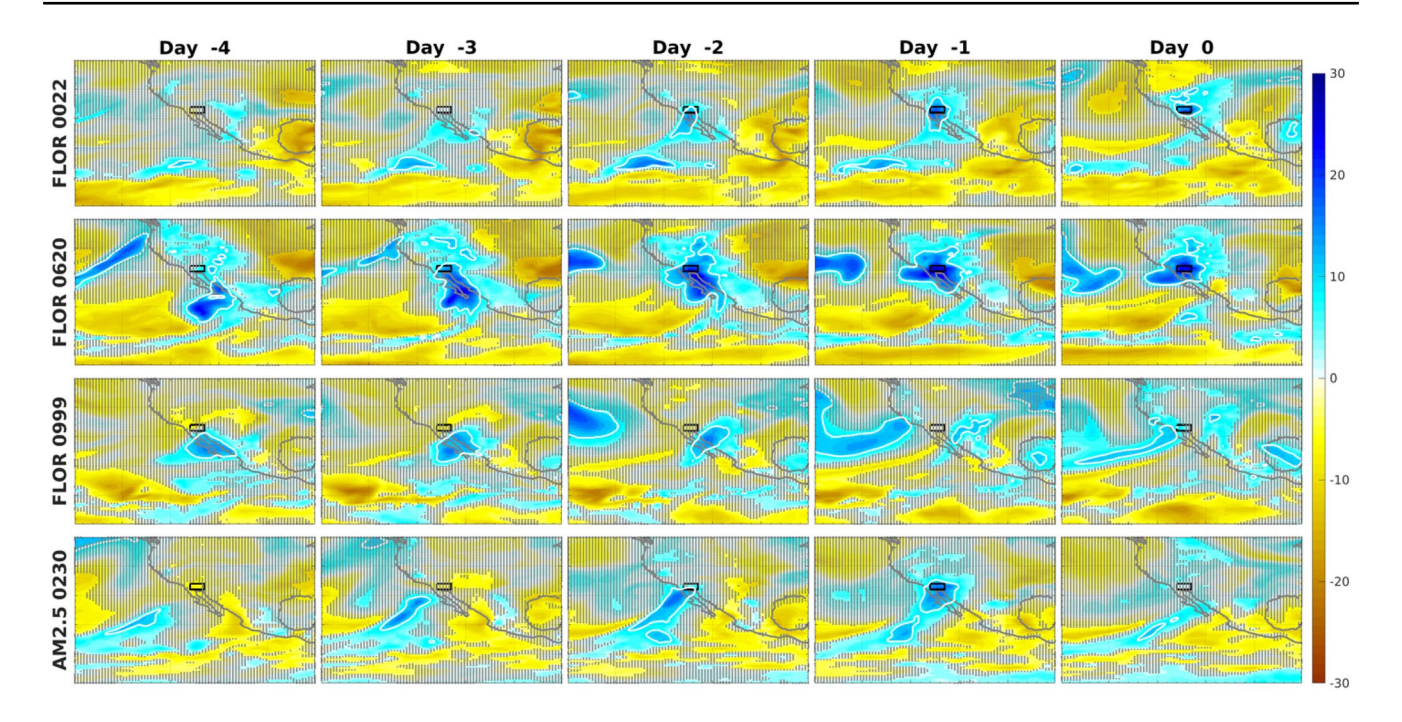


Fig. 6 Daily evolution of CWV anomalies (kg/m²) for four extreme events, FLOR 0022 (top row), 0620 (second row), 0999 (third row) and AM2.5 0230 (bottom row), from 4 days before the rainfall peak (left) to the peak (right). White contours denote the 10 kg/m² (i.e.,

1 cm) CWV anomalies. Gray stippling indicates that the CWV anomalies are within 2 standard deviations of June CWV daily variability (i.e., 95% confidence level assuming a normal distribution). The black box in each panel indicates the SWUNWM area

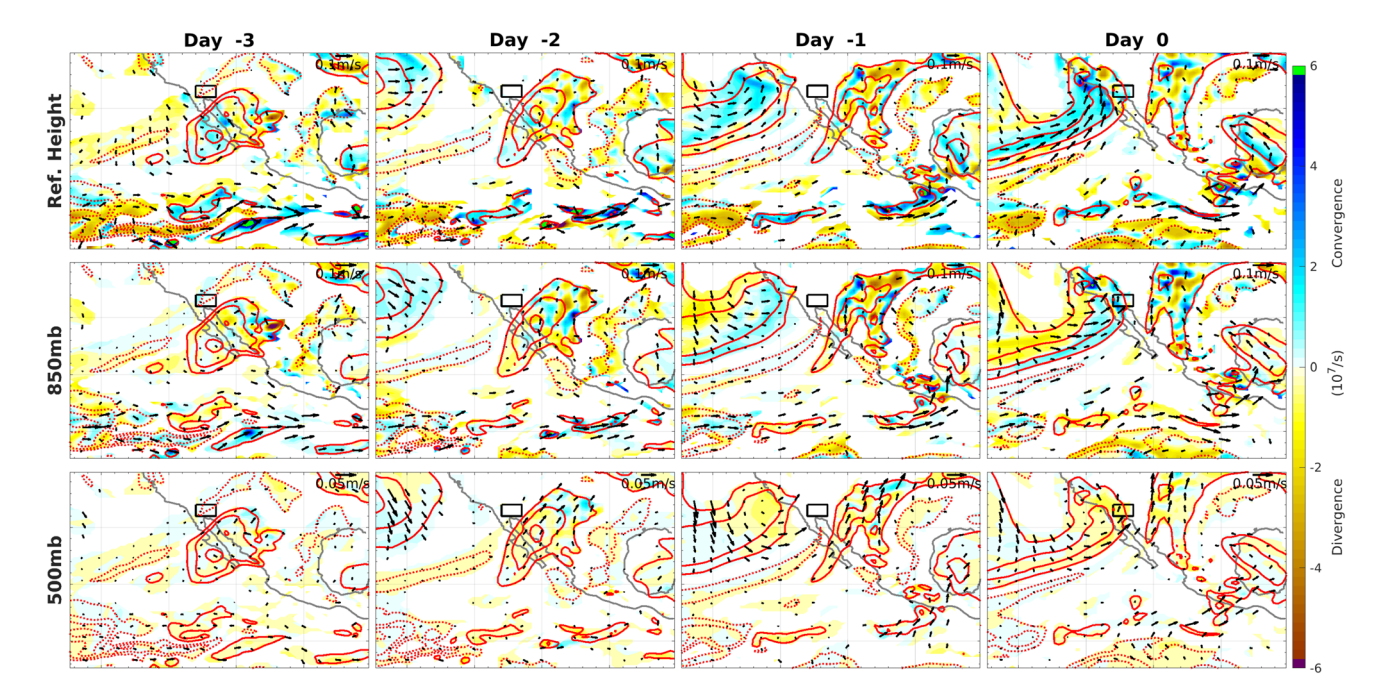


Fig. 7 Evolution of June extreme rainfall for Year 0999 in FLOR from 3 days before the rainfall peak (left-most column) to the peak (right-most column) at reference height (top row), 850 mb (middle row) and 500mb (bottom row). Red contours indicate the anomalous CWV with positive solid and negative dotted ($\pm 5~\text{kg/m}^2, \pm 10~\text{kg/m}^2, \pm 15~\text{kg/m}^2, \ldots$) and shading denotes the divergence of anomalous moisture fluxes in vectors. For clarity, moisture fluxes and their divergence are only plotted for the CWV anomalies larger than 2 standard

deviations of June CWV daily variability. For anomalous moisture fluxes, a scale vector of 0.1 m/s for reference height and 850 mb and 0.05 m/s for 500 mb is shown in the upper right corner in each panel. Note that moisture fluxes at reference height are calculated with 10 m winds and 2 m specific humidity. This case exemplifies the contribution of an AR (from northwest of SWUNWM, indicated by the black box in each panel) to the moisture associated with the extreme rainfall



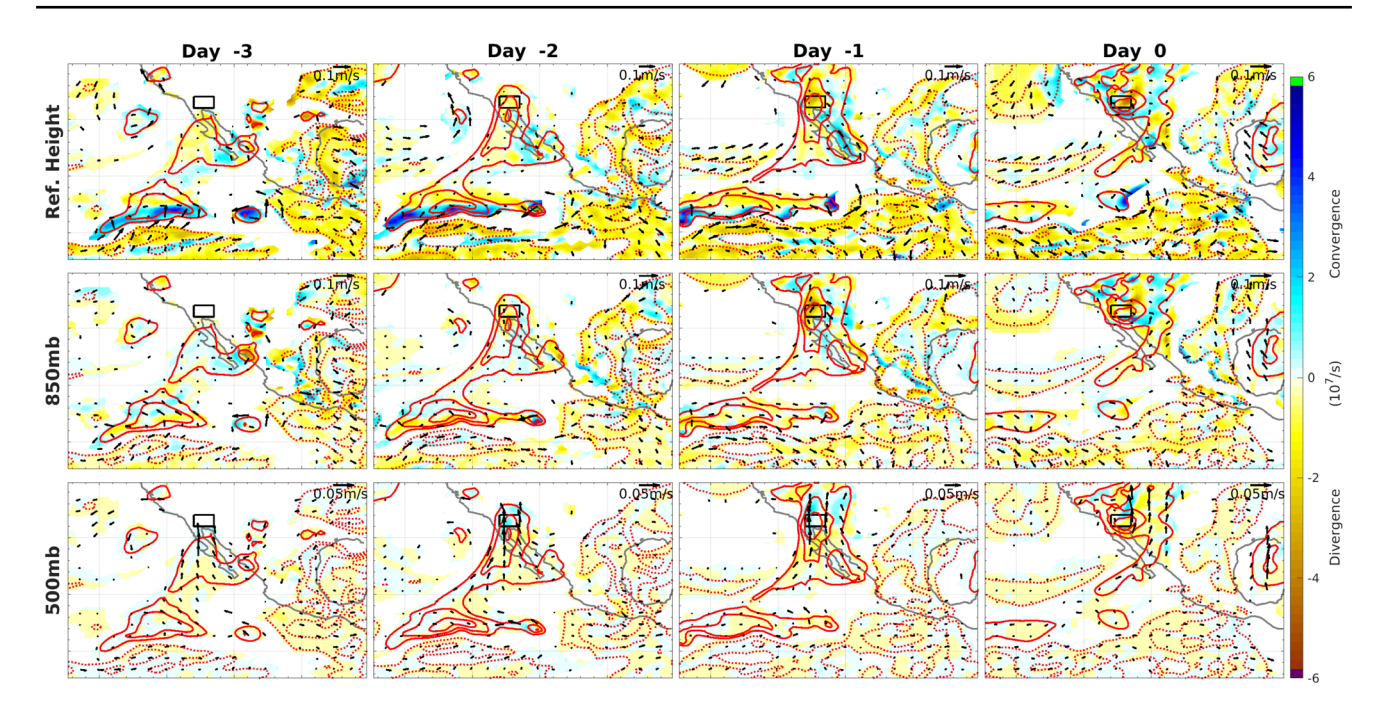


Fig. 8 The same as Fig. 7 but for Year 0022 in FLOR. This case exemplifies that, among the three levels shown here, 500 mb has the largest moisture contribution to the anomalous CWV associated with the extreme rainfall over SWUNWM

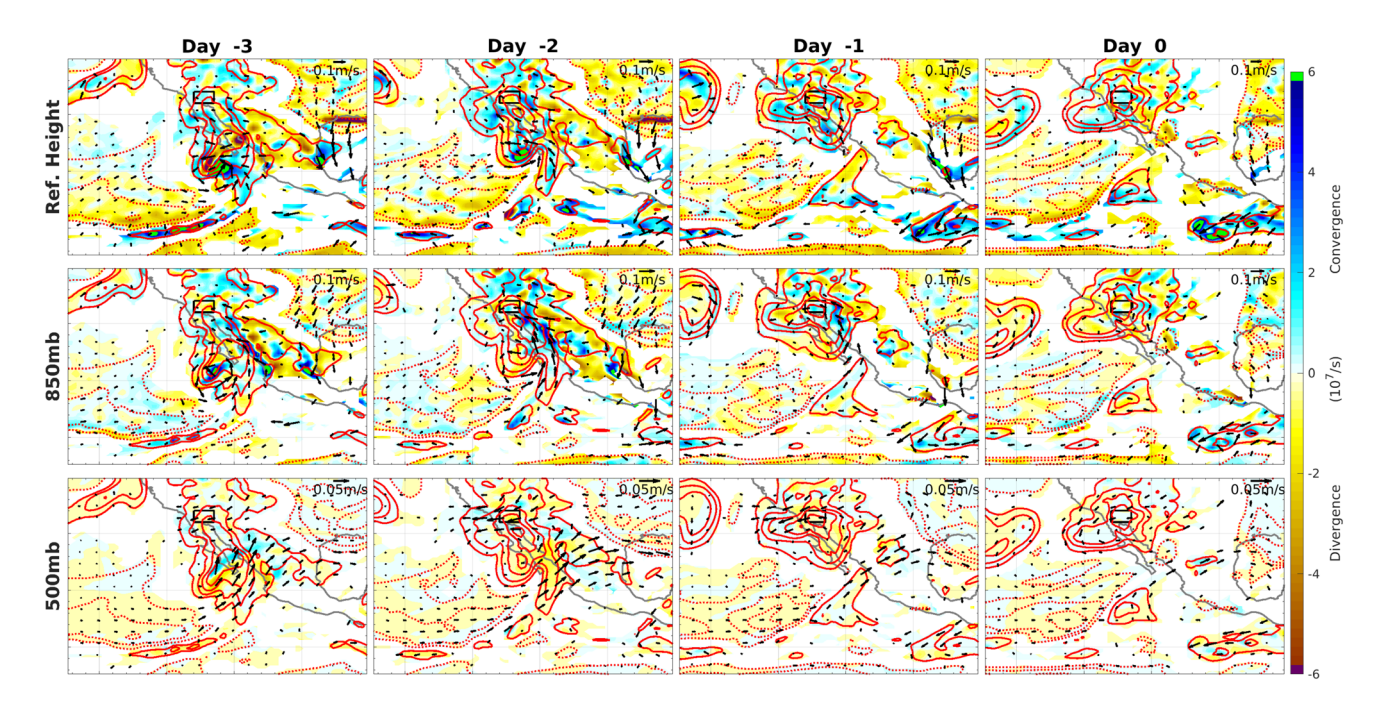


Fig. 9 The same as Fig. 7 but for Year 0620 in FLOR. This case exemplifies the contribution of TCs to the moisture associated with the extreme rainfall. The associated TC is located around 20°N and

115°W 3 days before the SWUNWM rainfall peak (see upper left panel) and formed around 12 N, 103 W about 9 days (not shown) before the rainfall peak

variance remains similar (Fig. 12f). These additional analyses from the 3500-year FLOR simulation provide cross validation for the conclusions above that SST variability affects the intensity of June extreme rainfall over SWUNWM via

its thermodynamic impacts on atmospheric moisture content, but does not appear to affect the rainfall occurrence (or frequency) that is dynamically controlled by atmospheric intrinsic processes.



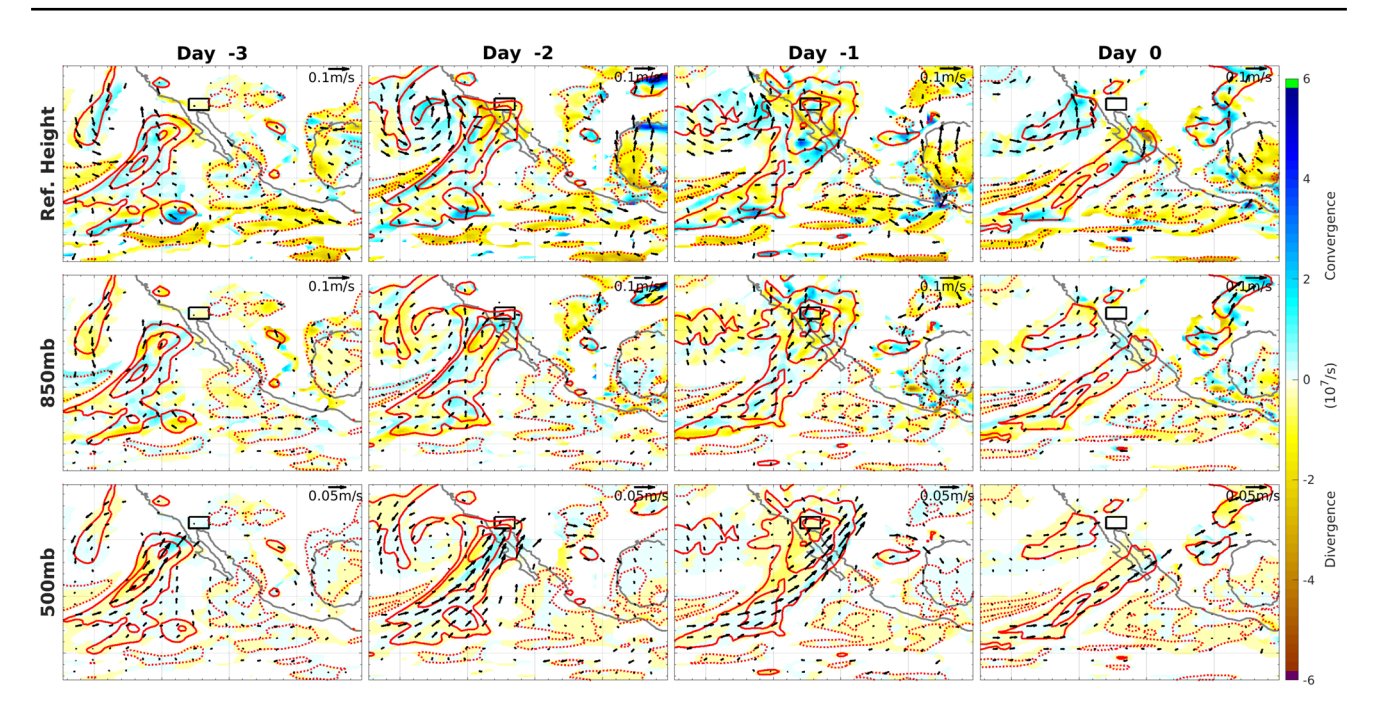


Fig. 10 The same as Fig. 7 but for Year 0230 in AM2.5. This case exemplifies the contribution of an AR (from southwest of SWUNWM) to the moisture associated with the extreme rainfall

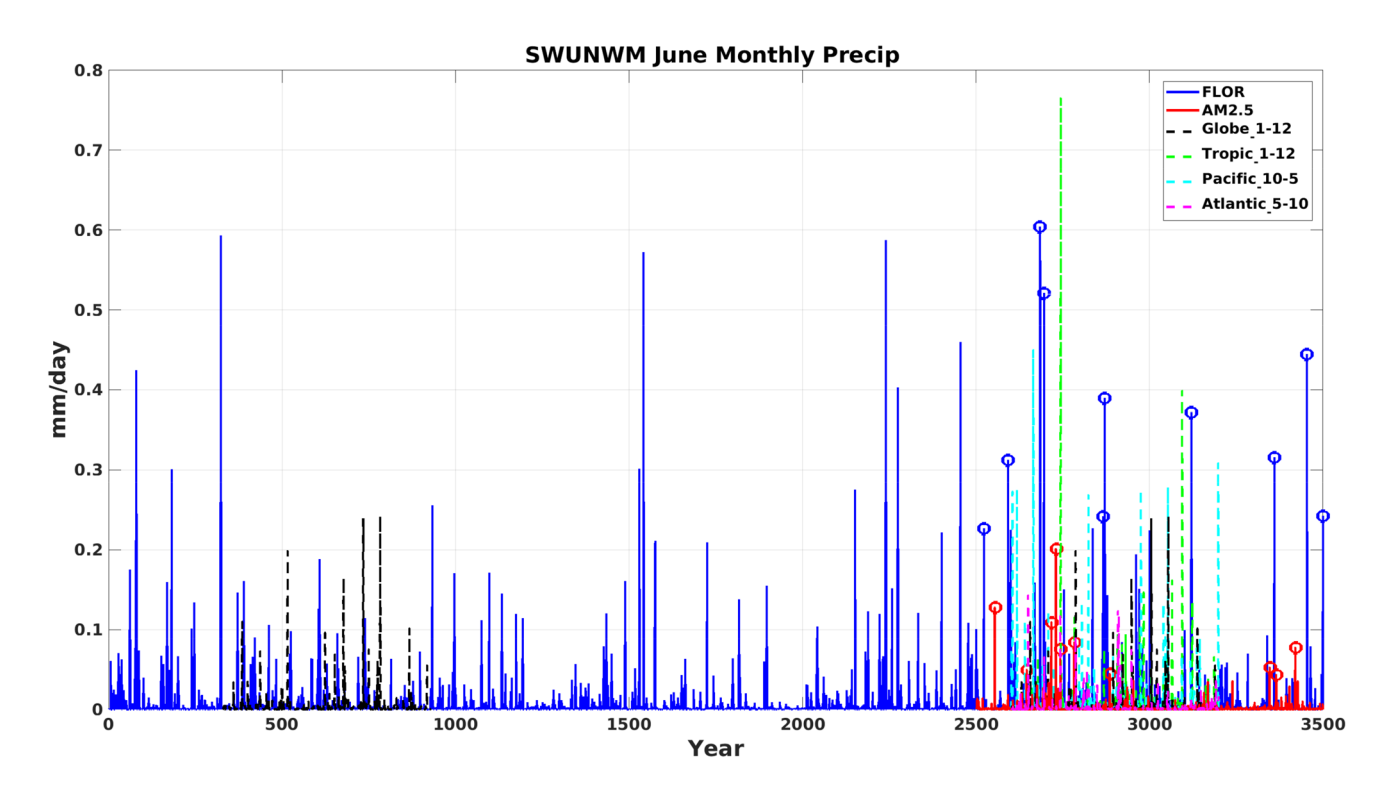


Fig. 11 The same as Fig. 2, but including the entire 3500-year FLOR and four idealized AM2.5 experiments with imposed monthly varying SST forcing from FLOR years 2601–3200 (see text for details): Globe_1-12 (dashed black), Tropic_1-12 (dashed green),

Pacific_10-5 (dashed cyan) and Atlantic_5-10 (dashed magenta). The Globe_1-12 time series is repeated over 0330-0929, during which FLOR simulates relatively weak June rainfall over SWUNWM



4 Conclusions and implications

In this work, we have used the GFDL global climate model FLOR to investigate the impacts of SST variability on extreme rainfall over the southwestern U.S. and northwestern Mexico area in June, the driest month of the year. Featuring a 50 km resolution in its atmosphere component AM2.5 and a fixed flux adjustment to reduce model mean biases, FLOR faithfully simulates the observed June rainfall climatology and variability on daily to interannual timescales over the SWUNWM area (despite its biases during other seasons). The performance of FLOR is further validated by process-level analysis regarding the June extreme rainfall over SWUNWM. Two millennium-long preindustrial simulations are conducted, one with the fully coupled FLOR and the other with the uncoupled AM2.5 (atmosphere is still coupled with land) forced by FLOR's climatological boundary conditions. These simulations differ only by the ocean, thus allowing a clean assessment of how the ocean affects June extreme rainfall over SWUNWM.

With millennium-long simulations, we have focused on the extreme rainfall events above the 99th percentile of June mean precipitation. Comparing the two simulations, we have found that while FLOR and AM2.5 simulate a similar 'most years extremely dry and occasionally relatively wet' interannual variation over SWUNWM, the intensity of June extreme rainfall is much stronger in FLOR than in AM2.5. Daily time series of these extreme rainfall shows that June extreme precipitation is mostly composed of one rainfall event lasting about one to a few days—a characteristic in both FLOR and AM2.5 (as well as in reanalysis product), but the overall amplitude of rainfall events is stronger in FLOR. A composite analysis of the daily evolution of June extreme rainfall events reveals that the pattern and magnitude of atmospheric circulation associated with the extreme rainfall are very similar between the two simulations (and reanalysis products), while the associated CWV anomalies are significantly larger in FLOR than in AM2.5. A further comparison of the variability in vertically integrated June mean atmospheric moisture content, lower tropospheric wind divergence and P-E (which combines the influences of atmospheric moisture and circulation) between the two simulations shows differences consistent with the composite analysis: compared to AM2.5, FLOR simulates stronger variability in CWV and P-E, but a similar magnitude of variability in vertically integrated wind divergence over the SWUNWM area. These results suggest that in FLOR the stronger intensity of June extreme rainfall over SWUNWM is a result of larger variability in atmospheric moisture content (and thus divergence of moisture fluxes) caused by SST variability, while the associated atmospheric circulation is

insensitive to SST variability and arises mainly from atmospheric intrinsic dynamics and atmosphere-land coupling.

The ocean affects atmospheric moisture content via evaporation and SST. A composite analysis of monthly mean SST anomalies associated with the extreme events in FLOR does not reveal any robust SST anomalies, suggesting that these extreme rainfall events are not associated with any specific SST variability. Four additional 600-year AM2.5 experiments are analyzed to provide further insights on the specific ocean regions crucial for the intensity of June extreme rainfall over SWUNWM. SST variations imposed in the tropical Pacific, including Globe_1-12, Tropic_1-12 and Pacific 10-5, are able to enhance the June CWV variability and intensify June extreme rainfall over SWUNWM, while those imposed only in the tropical Atlantic (during May to October) fail to do so. A caveat in Pacific_10-5 is that the imposed May SSTs are extrapolated into June, which precludes a clean assessment of the relative role of tropical Pacific SSTs in June versus the preceding months (October to May). Nonetheless, these results point strongly to a dominant role for the tropical Pacific variability in the intensity of June extreme rainfall over SWUNWM.

In Globe 1-12, the strongest June mean rainfall events over SWUNWM are somewhat weaker than those in the fully coupled FLOR as well as Tropic 1-12 and P10-15, but its CWV variability is enhanced and comparable to that in FLOR. This paradox is attributed to the dual dependence of rainfall on atmospheric moisture and circulation. Specifically, the atmospheric circulation associated with June extreme rainfall arises mainly from atmospheric intrinsic dynamics that are largely random. The random nature of atmospheric intrinsic dynamics allows extended dry and pluvial periods even for the same CWV variability. This behavior is simulated in both the 3500-year fully coupled FLOR and the 1000-year uncoupled AM2.5 without SST variability. The control of atmospheric intrinsic processes on rainfall dynamics also explains the similar temporal characteristics of June rainfall over SWUNWM between FLOR and AM2.5 shown in Fig. 2 (most years extremely dry and occasionally relatively wet) and Fig. 3 (June extreme rainfall mostly consists of one rainfall event lasting about one to a few days).

The modeling results presented here have important implications for June extreme rainfall over SWUNWM, particularly its intensity and occurrence. First of all, the intensity of June extreme rainfall depends crucially on SST variability. A reliable simulation and prediction of the intensity of June extreme rainfall over SWUNWM requires a faithful representation of SST variability, especially in the tropical Pacific. Second, the insensitivity of atmospheric circulation associated with June extreme rainfall to SST variability, and the similar temporal characteristics of June precipitation between FLOR and AM2.5 on both daily and interannual time scales, suggest that the processes controlling when June extreme rainfall occurs



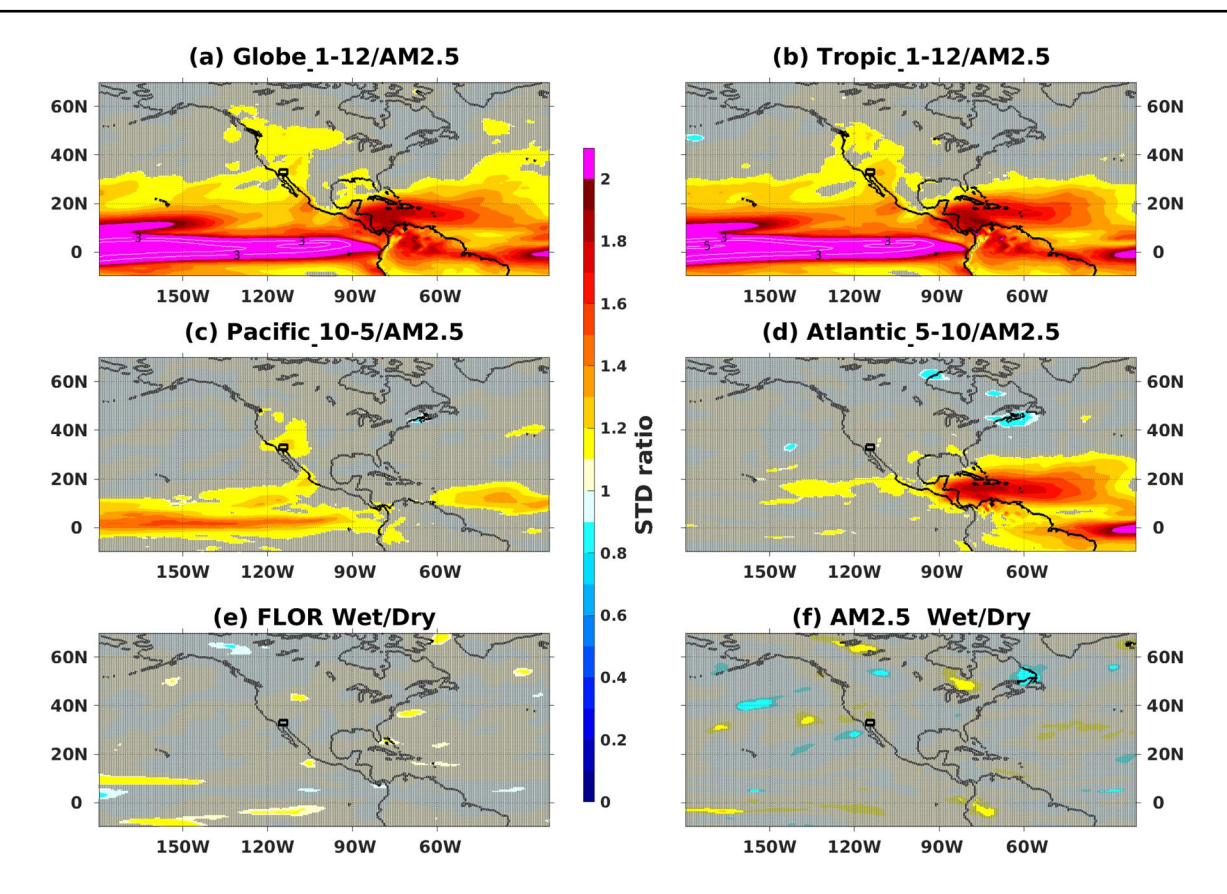


Fig. 12 The ratio of June CWV standard deviation in **a** Globe_1-12, **b** Tropic_1-12, **c** Pacific_10-5 and **d** Atlantic_5-10 against AM2.5 (the same as Fig. 5a); in **e** FLOR between 2501–3500 (wet) and 0451–1450 (dry) and **f** AM2.5 between 0001–0400 (wet) and 0451–0850 (dry). The wet and dry periods in **e**, **f** are based on the

SWUNWM June rainfall (see Fig. 11). Ratios larger than 2 are contoured in white. Gray stippling indicates that the standard deviation is not significantly different at the 1% significance level based on the F test. The SWUNWM area is indicated in each panel by a black box

over SWUNWM mainly arise from atmospheric intrinsic dynamics and atmosphere-land coupling. An implication is that the predictability of the occurrence of June extreme rainfall over SWUNWM is limited by atmospheric intrinsic dynamics and atmosphere-land coupling.

Acknowledgements H. Zhang conducted the experiments at Princeton University while being supported under block funding from NOAA/GFDL, and carried out the analysis at Lamont Doherty Earth Observatory of Columbia University while being supported by NSF award OCE-16-57209 and NSF award AGS-19-34363. H. Zhang is grateful for Tom Delworth's continuous support after his postdoctoral training at GFDL. H. Zhang is especially grateful for Richard Seager's generous support on developing his personal research interests, as exemplified

by this work. Comments from Richard Seager, Tom Delworth and two anonymous reviewers greatly improve the manuscript. GPCC and CPC US Unified Precipitation data are provided by the NOAA/OAR/ESRL PSD, Boulder, Colorado, USA, from their Web site at https://www.esrl.noaa.gov/psd/. All modeling data used here are archived on Lamont data server and access will be available upon request.

Appendix

See Figs. 13, 14, 15, 16 and 17 and Table 1.



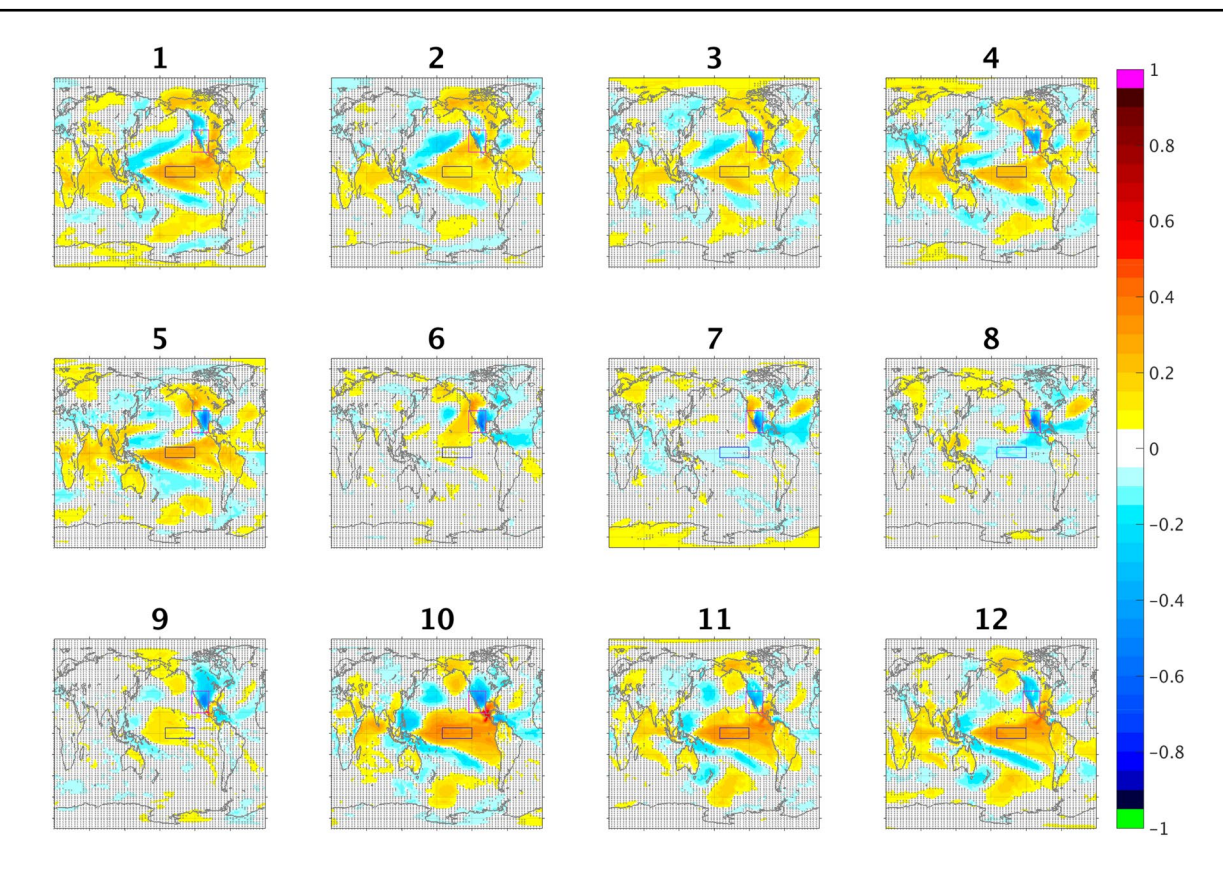


Fig. 13 Correlation of monthly surface temperature with monthly precipitation averaged over southwestern North America (19–40 $^{\circ}$ N, 125–96 $^{\circ}$ W, indicated by a red box in each panel) as a function of cal-

endar months in FLOR. Gray stippling denotes that the correlation is not significant at 5% level (based on a two-sided student *t* test)

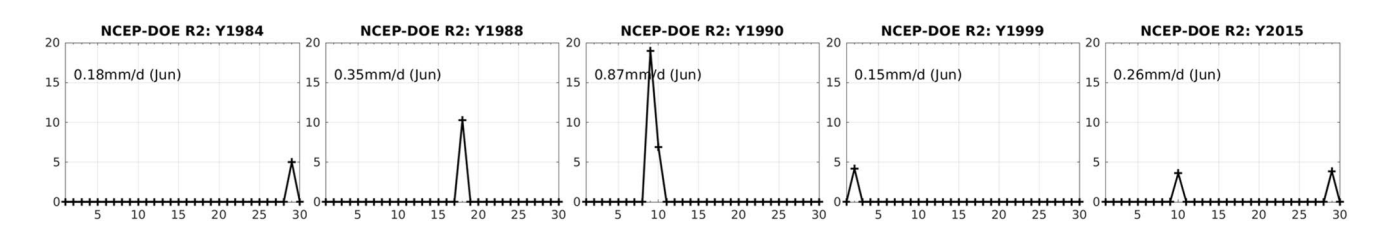


Fig. 14 Daily time series of selected June rainfall over SWUNWM in the NCEP-DOE reanalysis II product. The product is on a global T62 Gaussian grid. Plotted here are the five strongest years (see title in each panel) based on the total June rainfall amount (labeled in

each panel) during 1979–2019. Note that these events represent the top 12.5% (5/40) events during the reanalysis period and are selected somewhat randomly since the 1% criterion from the model is not applicable in the reanalysis owing to its small number of samples

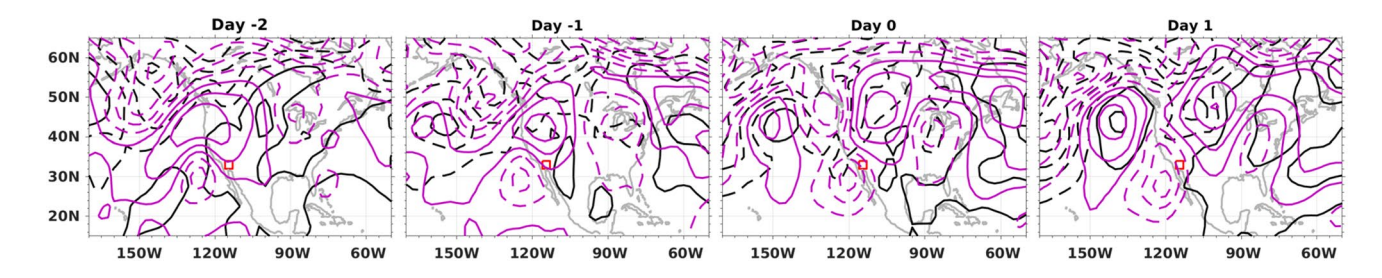


Fig. 15 Composite evolution of SLP and 500GH for the NCEP-DOE reanalysis events shown in Fig. 14, with contours convention the same as Fig. 4 in the main text. The red box in each panel indicates the SWUNWM region



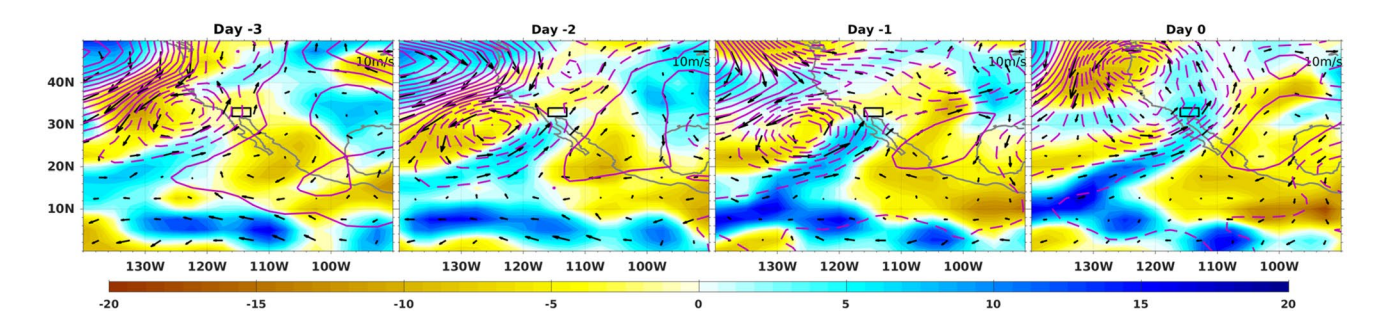


Fig. 16 Evolution of the rainfall event peaked on June 2, 1999 (Day 0) in the NCEP-DOE reanalysis shown in Fig. 14. Shading indicates CWV anomalies (kg/m^2) , contours show 500 mb geopotential height anomalies $(\pm 10 \text{ m}, \pm 30 \text{ m}, \pm 50 \text{ m}, \dots \text{ positive solid and negative dashed)}$ and arrows denote 500 mb wind anomalies with a scale vector of 10 m/s in the upper right corner. The SWUNWM area is indi-

cated in each panel by a black box. This rainfall event appears to be associated with an AR propagating from southwest of the SWUNWM area. The AR is located at the southern flank of the anomalous cyclone (centered around 125 W, 35 N on Day -3) and features a narrow band of anomalous positive CWV and southwesterly winds

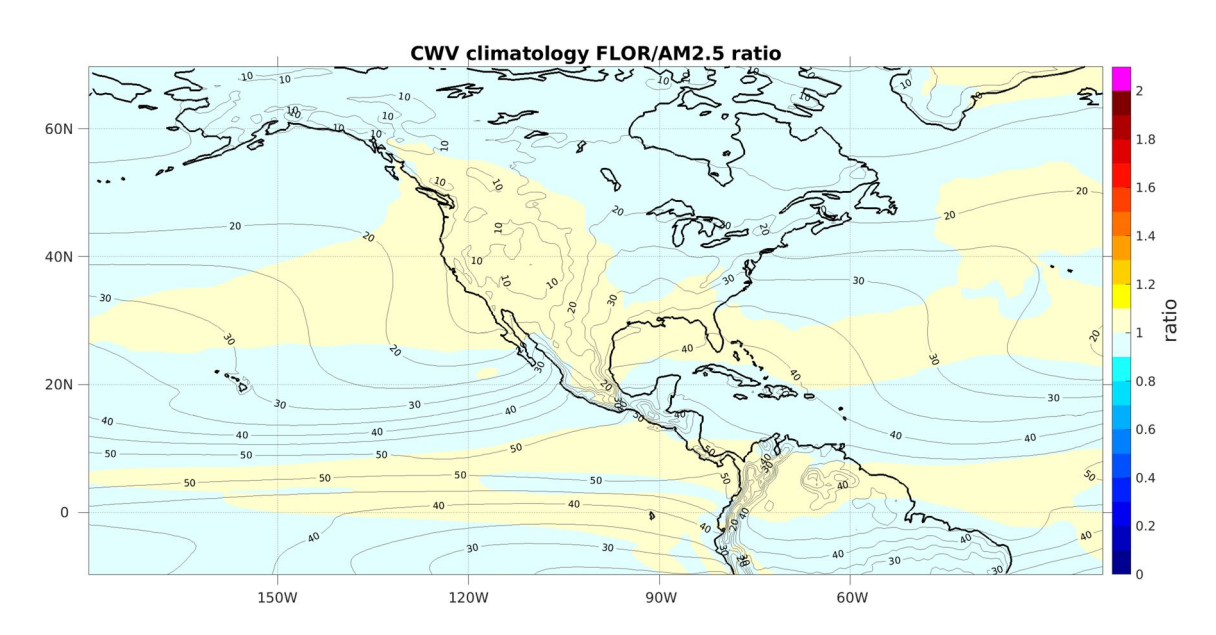


Fig. 17 FLOR to AM2.5 ratio of June CWV climatology (shading) and the FLOR CWV climatology (gray contours, in kg/m²). The ratio ranges from 0.93 to 1.07. Note that the color range is chosen to highlight the similarity between FLOR and AM2.5 in their CWV climatology



Table 1 Summary of moisture sources for June extreme rainfall events and contributions from reference height (10 m winds and 2 m specific humidity), 850mb and 500mb based on the evolution of associated daily mean CWV and moisture flux anomalies in FLOR and AM2.5

FLOR					AM2.5				
Year	CWV	Reference	850 mb	500 mb	Year	CWV	Reference	850 mb	500 mb
0022	S, D-3	NOC	NOC	S, D-3~0	0054	SE, D-2	E, D-2~-1	SE, D-2~-1	WC
0092	S, D-3	N, D-3; NS, D-2, S, D-1	SE, D0	NE, D-3~-2; E, D-1	0146	SE, D-3	E, D-1~0	SEE, D-2~-1	SE, D-2
0184	SE, D-3	SEE, D-3~-2; NEE, D-1	SE, D-3~0	SW, D-3 ~ -2; S, D-1	0217	SE, D-5	D-4~-3; E, D-2~0	D-4~-1; S, D0	WC
0195 TC	SE, D-3	SSE, D-3~-1	ESE, D0	E, D-1 \sim 0	0230 AR	SW, D-4	S, D-1	SW, D-2~-1	SW, D-3
0365	SE, D-3	NEE, D-3 ~ -2; SEE, D-1 ~ 0	NEE, D-3~-2	E, D-2~-1	0243	E, D-4	E, D-4~-1; SE, D0	E, D-4~-2	WC
0370 TC	SE, D-3	NEE, D-2; E/ SE, D-1	NE, D-2; E, D-1; NW, D0	NE, D-1	0283 AR	SW, D-4	D-2~0	D-2~0	SSW, D-3~-2
0620 TC	E/SE, D-3	E/SE, D-4~-3; SE, D-0	E, D-2~-1	NE, D-4~-3,	0385	SW, D-2	NOC	D-1	S, D-2~-1
0859	SE, D-4	E, D-3~0	NE/E/SE, D-3~-1	NOC	0846	S, D-2	N, D-3; S, D-2~0	S, D-1	NOC
0953	NW, D-5; SE, D-2	SE, D-1	SE, D-1	SSE, D-3~-1	0865	SE, D-3	SE, D-1~0	SE, D-1	SE, D0
0999 AR	W/NW, D-1	S/SE, D0	S/SW, D0	SW, D-1	0920	SE, D-4	E, D-2~0	E, D-2~0	NOC

Symbols used in the table are defined as follows. S: south, N: north, E: east, W: west (whereabouts); D: day (time); NOC: no obvious contribution, WC: weak contribution (moisture contribution); TC: tropical cyclone, AR: atmospheric river (event type). For each event, the table summarizes where and when the total moisture (CWV) anomaly over SWUNWM appears to come from and on each level where the moisture fluxes appear to come from and when they converge over SWUNWM. Take Year 0022 in FLOR for example, 'S, D-3' means that the CWV anomaly appears to come from the south 3 days before the rainfall peak, with no obvious contributions at reference height and 850 mb ('NOC') but noticeable southerly moisture flux convergence at 500 mb lasting from 3 days before the peak to the peak ('S, D-3~0'). The whereabouts and time information of moisture flux convergence on the three levels are not given in cases they are not obvious based on visual examination. The events that appear to result from tropical cyclones or atmospheric rivers are labeled TC or AR in bold next to their Years

References

- Adams DK, Comrie AC (1997) The North American Monsoon. Bull Am Meteorol Soc 78:2197–2214. https://doi.org/10.1175/1520-0477(1997)078%3c2197:TNAM%3e2.0.CO;2
- Andrews ED, Antweiler RC, Neiman PJ, Ralph FM (2004) Influence of ENSO on flood frequency along the California Coast. J Climate 17:337–348. https://doi.org/10.1175/1520-0442(2004)017%3c0337:IOEOFF%3e2.0.CO;2
- Bao J-W, Michelson SA, Neiman PJ et al (2006) interpretation of enhanced integrated water vapor bands associated with extratropical cyclones: their formation and connection to tropical moisture. Mon Weather Rev 134:1063–1080. https://doi. org/10.1175/MWR3123.1
- Bracken C, Rajagopalan B, Alexander M, Gangopadhyay S (2015) Spatial variability of seasonal extreme precipitation in the western United States. J Geophys Res Atmos 120:4522–4533. https://doi.org/10.1002/2015JD023205
- Cannon AJ (2015) Revisiting the nonlinear relationship between ENSO and winter extreme station precipitation in North America. Int J Climatol 35:4001–4014. https://doi.org/10.1002/joc.4263
- Cannon F, Hecht CW, Cordeira JM, Ralph FM (2018) Synoptic and mesoscale forcing of Southern California extreme precipitation. J Geophys Res Atmos 123:13,714–13,730. https://doi. org/10.1029/2018JD029045

- Corringham TW, Cayan DR (2019) The effect of El Niño on flood damages in the Western United States. Weather Climate Soc 11:489–504. https://doi.org/10.1175/WCAS-D-18-0071.1
- Curtis S (2008) The Atlantic multidecadal oscillation and extreme daily precipitation over the US and Mexico during the hurricane season. Climate Dyn 30:343–351. https://doi.org/10.1007/s0038 2-007-0295-0
- Dettinger M (2013) Atmospheric rivers as drought busters on the U.S. West Coast. J Hydrometeorol 14:1721–1732. https://doi.org/10.1175/JHM-D-13-02.1
- Dettinger M (2016) Historical and future relations between large storms and droughts in California. San Francisco Estuary and Watershed Science 14
- Dettinger M, Ralph FM, Das T et al (2011) Atmospheric rivers, floods and the water resources of California. Water 3:445–478. https://doi.org/10.3390/w3020445
- Eckhardt S, Stohl A, Wernli H et al (2004) A 15-year climatology of warm conveyor belts. J Climate 17:218–237. https://doi.org/10.1175/1520-0442(2004)017%3c0218:AYCOW C%3e2.0.CO;2
- Grantz K, Rajagopalan B, Clark M, Zagona E (2007) Seasonal shifts in the North American Monsoon. J Climate 20:1923–1935. https://doi.org/10.1175/JCLI4091.1
- Harris I, Jones P, Osborn T, Lister D (2014) Updated high-resolution grids of monthly climatic observations—the CRU TS3.10 Dataset. Int J Climatol 34:623–642. https://doi.org/10.1002/joc.3711



- He J, Deser C, Soden BJ (2017) Atmospheric and oceanic origins of tropical precipitation variability. J Climate 30:3197–3217. https://doi.org/10.1175/JCLI-D-16-0714.1
- He J, Kirtman B, Soden BJ et al (2018) Impact of ocean eddy resolution on the sensitivity of precipitation to CO₂ increase. Geophys Res Lett 45:7194–7203. https://doi.org/10.1029/2018GL078235
- Higgins RW, Schemm J-KE, Shi W, Leetmaa A (2000) Extreme precipitation events in the Western United States related to tropical forcing. J Climate 13:793–820. https://doi.org/10.1175/1520-0442(2000)013%3c0793:EPEITW%3e2.0.CO;2
- Hoskins BJ, Karoly DJ (1981) The steady linear response of a spherical atmosphere to thermal and orographic forcing. J Atmos Sci 38:1179–1196. https://doi.org/10.1175/1520-0469(1981)038%3c1179:TSLROA%3e2.0.CO;2
- Jia L, Yang X, Vecchi GA et al (2014) Improved seasonal prediction of temperature and precipitation over land in a high-resolution GFDL climate model. J Climate 28:2044–2062. https://doi.org/10.1175/ JCLJ-D-14-00112.1
- Jones C, Carvalho LMV (2012) Spatial-intensity variations in extreme precipitation in the contiguous United States and the Madden–Julian oscillation. J Climate 25:4898–4913. https://doi. org/10.1175/JCLI-D-11-00278.1
- Jones C, Carvalho LMV (2014) Sensitivity to Madden–Julian oscillation variations on heavy precipitation over the contiguous United States. Atmos Res 147–148:10–26. https://doi.org/10.1016/j.atmosres.2014.05.002
- Jones C, Carvalho LMV, Gottschalck J, Higgins W (2011) The Madden–Julian oscillation and the relative value of deterministic forecasts of extreme precipitation in the contiguous United States. J Climate 24:2421–2428. https://doi.org/10.1175/2011JCLI-D-10-05002.1
- Jones C, Gottschalck J, Carvalho LMV, Higgins W (2010) Influence of the Madden–Julian oscillation on forecasts of extreme precipitation in the contiguous United States. Mon Weather Rev 139:332– 350. https://doi.org/10.1175/2010MWR3512.1
- Kanamitsu M, Ebisuzaki W, Woollen J et al (2002) NCEP–DOE AMIP-II reanalysis (R-2). Bull Am Meteorol Soc 83:1631–1644. https:// doi.org/10.1175/BAMS-83-11-1631
- Lahmers TM, Castro CL, Adams DK et al (2016) Long-term changes in the climatology of transient inverted troughs over the North American Monsoon region and their effects on precipitation. J Climate 29:6037–6064. https://doi.org/10.1175/JCLI-D-15-0726.1
- Moore BJ, Neiman PJ, Ralph FM, Barthold FE (2011) Physical processes associated with heavy flooding rainfall in Nashville, Tennessee, and vicinity during 1–2 may 2010: the role of an atmospheric river and mesoscale convective systems. Mon Weather Rev 140:358–378. https://doi.org/10.1175/MWR-D-11-00126.1
- Neiman PJ, Schick LJ, Ralph FM et al (2011) Flooding in Western Washington: the connection to atmospheric rivers. J Hydrometeorol 12:1337–1358. https://doi.org/10.1175/2011JHM1358.1
- Notaro M, Liu Z, Gallimore RG et al (2010) Complex seasonal cycle of ecohydrology in the Southwest United States. J Geophys Res Biogeosci. https://doi.org/10.1029/2010JG001382
- Pascale S, Boos WR, Bordoni S et al (2017) Weakening of the North American monsoon with global warming. Nat Climate Change 7:806. https://doi.org/10.1038/nclimate3412
- Pascale S, Bordoni S, Kapnick SB et al (2016) The impact of horizontal resolution on North American Monsoon Gulf of California moisture surges in a suite of coupled global climate models. J Climate 29:7911–7936. https://doi.org/10.1175/JCLI-D-16-0199.1
- Pascolini-Campbell M, Seager R, Williams AP et al (2019) Dynamics and variability of the spring dry season in the United States

- Southwest as observed in AmeriFlux and NLDAS-2 Data. J Hydrometeorol 20:1081–1102. https://doi.org/10.1175/JHM-D-18-0154.1
- Ralph FM, Coleman T, Neiman PJ et al (2012) Observed impacts of duration and seasonality of atmospheric-river landfalls on soil moisture and runoff in Coastal Northern California. J Hydrometeorol 14:443–459. https://doi.org/10.1175/JHM-D-12-076.1
- Ralph FM, Neiman PJ, Wick GA (2004) Satellite and CALJET aircraft observations of atmospheric rivers over the Eastern North Pacific Ocean during the Winter of 1997/98. Mon Weather Rev 132:1721–1745. https://doi.org/10.1175/1520-0493(2004)132%3c1721:SACAOO%3e2.0.CO:2
- Ralph FM, Neiman PJ, Wick GA et al (2006) Flooding on California's Russian River: role of atmospheric rivers. Geophys Res Lett. https://doi.org/10.1029/2006GL026689
- Ruprich-Robert Y, Delworth T, Msadek R et al (2018) Impacts of the Atlantic multidecadal variability on North American Summer climate and heat waves. J Climate 31:3679–3700. https://doi.org/10.1175/JCLI-D-17-0270.1
- Schneider U, Becker A, Finger P et al (2011) GPCC Full data reanalysis version 6.0 at 0.5°: monthly land-surface precipitation from rain-gauges built on GTS-based and historic data. https://doi.org/10.5676/DWD_GPCC/FD_M_V7_050
- Schubert SD, Chang Y, Suarez MJ, Pegion PJ (2008) ENSO and Wintertime extreme precipitation events over the contiguous United States. J Climate 21:22–39. https://doi.org/10.1175/2007JCLI17 05.1
- Seager R, Henderson N (2013) Diagnostic computation of moisture budgets in the ERA-interim reanalysis with reference to analysis of CMIP-archived atmospheric model data. J Climate 26:7876– 7901. https://doi.org/10.1175/JCLI-D-13-00018.1
- Shepherd TG (2014) Atmospheric circulation as a source of uncertainty in climate change projections. Nat Geosci 7:703–708. https://doi.org/10.1038/ngeo2253
- Sierks MD, Kalansky J, Cannon F, Ralph FM (2020) Characteristics, origins, and impacts of summertime extreme precipitation in the Lake Mead Watershed. J Climate 33:2663–2680. https://doi. org/10.1175/JCLI-D-19-0387.1
- Stan C, Straus DM, Frederiksen JS et al (2017) Review of tropicalextratropical teleconnections on intraseasonal time scales. Rev Geophys 55:902–937. https://doi.org/10.1002/2016RG000538
- Vecchi GA, Delworth T, Gudgel R et al (2014) On the seasonal forecasting of regional tropical cyclone activity. J Climate 27:7994– 8016. https://doi.org/10.1175/JCLI-D-14-00158.1
- Zhang H, Delworth T, Zeng F et al (2016) Detection, attribution, and projection of regional rainfall changes on (multi-) decadal time scales: a focus on Southeastern South America. J Climate 29:8515–8534. https://doi.org/10.1175/JCLI-D-16-0287.1
- Zhang H, Delworth TL (2018a) Robustness of anthropogenically forced decadal precipitation changes projected for the 21st century. Nat Commun 9:1150. https://doi.org/10.1038/s41467-018-03611-3
- Zhang H, Delworth TL (2018b) Detectability of decadal anthropogenic hydroclimate changes over North America. J Climate 31:2579–2597. https://doi.org/10.1175/JCLI-D-17-0366.1
- Zheng C, Kar-Man Chang E, Kim H-M et al (2018) Impacts of the Madden–Julian oscillation on storm-track activity, surface air temperature, and precipitation over North America. J Climate 31:6113–6134. https://doi.org/10.1175/JCLI-D-17-0534.1

Publisher's Note Springer Nature remains neutral with regard to jurisdictional claims in published maps and institutional affiliations.

